



This work was carried out in whole or in part within the framework of the NOMATEN Center of Excellence, supported from the European Union Horizon 2020 research and innovation programme (Grant Agreement No. 857470) and from the European Regional Development Fund via the Foundation for Polish Science International Research Agenda PLUS programme (Grant No. MAB PLUS/2018/8).

This is a copy of the publication which appeared in *Vacuum*, Volume 219, Part A, January 2024, 112733, published on: 29 October 2023.

DOI: [10.1016/j.vacuum.2023.112733](https://doi.org/10.1016/j.vacuum.2023.112733)



Atomistic insights into nanoindentation-induced deformation of α -Al₂O₃ single crystals

Qinqin Xu^a, Agata Zaborowska^a, Katarzyna Mulewska^a, Wenyi Huo^{a,b,*}, Kamran Karimi^a, F. Javier Domínguez-Gutiérrez^a, Łukasz Kurpaska^a, Mikko J. Alava^{a,c}, Stefanos Papanikolaou^{a,*}

^a NOMATEN Centre of Excellence, National Centre for Nuclear Research, ul. A. Soltana 7, 05-400 Otwock, Poland

^b College of Mechanical and Electrical Engineering, Nanjing Forestry University, 210037 Nanjing, China

^c Department of Applied Physics, Aalto University, P.O. Box 11000 00076 Aalto, Espoo, Finland

ARTICLE INFO

Keywords:

α -Al₂O₃
Dislocation dynamics
Mechanical behaviors
Nanoindentation
Phase transformation
Molecular dynamics

ABSTRACT

The plastic deformability of brittle ceramics, e.g., Al₂O₃, at a small scale can expand their potential structural applications. In this work, we propose to investigate the nanomechanics and plasticity of α -Al₂O₃ using molecular dynamics (MD) simulations at room temperature. First, nanoindentation MD simulations are performed with single crystalline α -Al₂O₃. Four crystallographic orientations are investigated, *m* [1100], *a* [2 $\bar{1}\bar{1}$ 0], *R* [$\bar{1}$ 012] and *c* [0001], including a detailed analysis of Al₂O₃ dislocation-based mechanisms. The results show that the O atoms undergo a phase transformation, changing from the hexagonal close-packed structure to face-centered cubic and body-centered cubic structures. Second, during nanoindentation, we focus on pop-in events and the transformation point from elastic to inelastic response during loading forces. The results are discussed in the context of recent transmission electron microscope experiments, possibly opening new doors towards ceramic bulk material processes.

1. Introduction

Alumina is the second most abundant metal oxide of the Earth's crust next to silica. There are various polymorphs, e.g., α , β , γ , η , θ , δ , κ and χ -Al₂O₃. Among them, α -Al₂O₃, i.e., corundum, is phase-stable and widely concerned. It has been applied as a coating material on mechanical components, due to its outstanding mechanical properties [1]. At room temperature (RT), α -Al₂O₃ can be plastically deformed, under hydrostatic pressure sufficient to inhibit cracking and used to increase the crack growth rate into the deep oxidation zone in several materials [2]. The material characterization and its deformation mechanisms during micro-indentation have been studied by transmission and scanning electron microscopy (TEM) [3]. Dislocation slip and twinning are proposed as the dominant deformation mechanisms [4,5]. During mechanical polishing, there are high densities of dislocations produced within the nearly polished surface [3]. On the other hand, the dominant deformation mechanism changes to slip and mechanical twinning during the placement of Vickers microhardness indentations [3,5]. Unlike the deformation of ductile metals, that of brittle oxides is considered to be a result of local stresses [6]. The effect of local stress is even stronger when the brittle oxides are tested using nanoindentation, the technique of measuring the mechanical properties at very small scales [7,8].

In the field of mechanical engineering, molecular dynamics (MD) simulations are a valuable tool for studying the dynamic deformation behavior of materials under different loading conditions. This is particularly useful, as such behavior can be challenging to investigate experimentally. Combined with MD simulations, the deformation mechanism, especially the dislocation-related activity, is further revealed [9]. In α -Al₂O₃, the local structures and energy for dissociation of the basal edge dislocations into partial dislocations were studied and were in good agreement with the TEM results [10]. MD simulations are recognized to play important roles in unveiling deformation mechanisms that are not easily accessible experimentally. The ideal strength of α -Al₂O₃ was proposed using the density functional theory (DFT) method [11]. It is much higher than that of θ -Al₂O₃ due to its highly ionic Al–O bonds. On the other hand, especially for dislocation analysis during nanoindentation in α -Al₂O₃, the DFT method can hardly be applicable since indentation models larger than 10 nm may involve more than 100,000 atoms [10]. Experimentally, highly textured α -Al₂O₃ samples were studied [12]. The samples with perfect orientations exhibited excellent mechanical properties when compared to a randomly textured α -Al₂O₃ sample. Unfortunately, there is still a lack of information on the atomic deformation mechanism of α -Al₂O₃ with different orientations during nanoindentation.

* Corresponding author at: NOMATEN Centre of Excellence, National Centre for Nuclear Research, ul. A. Soltana 7, 05-400 Otwock, Poland.

E-mail addresses: wenyi.huo@ncbj.gov.pl (W. Huo), stefanos.papanikolaou@ncbj.gov.pl (S. Papanikolaou).

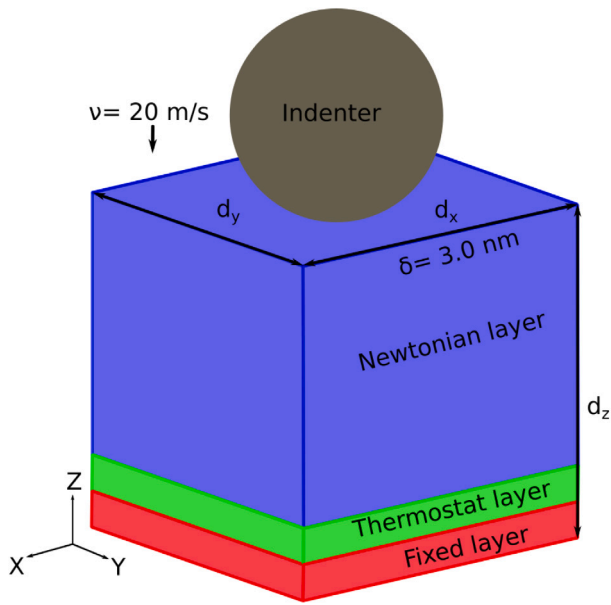


Fig. 1. Schematic of the MD simulation model for the nanocontact between a spherical indenter tip and an α - Al_2O_3 sample.

Herein, nanoindentation responses of four typical orientations of single crystalline α - Al_2O_3 are investigated using MD simulations, m $[1\bar{1}00]$, a $[2\bar{1}\bar{1}0]$, R $[\bar{1}012]$ and c $[0001]$, including a detailed dislocation evolution analysis. First, we describe the computational methodology for performing nanoindentation simulations and sample preparation. Then, we present the results for dislocation nucleation and defect nucleation mechanisms. Finally, concluding remarks are summarized.

2. Computational methods

The sketch in Fig. 1 schematically shows the single crystalline α - Al_2O_3 sample under nanoindentation. The indentation setup includes a simulation cell with dimensions. It is built up with a cell size of $25.2 \text{ nm} \times 23.8 \text{ nm} \times 27.7 \text{ nm}$ (length \times height \times width) consisting of approximately 2×10^6 atoms. The lattice parameters are $a_0 = 4.27 \text{ \AA}$ and $c_0 = 13.17 \text{ \AA}$ which are determined from experiments and first-principles simulations [13]. Three layers exist in the model along the Z direction, as shown in Fig. 1. Periodic boundary conditions are applied to the X and Y directions, while the Z direction is imposed by a fixed boundary condition. The fixed layers ($0.02d_z$) of the substrate are fixed to prevent the rigid-body translation. The thermostat region ($0.08d_z$) is placed above the fixed region to absorb the excessive heat generated during the test. The temperature in the thermostat region is controlled using the Langevin thermostat, while the remaining region follows the atomic motions governed by Newton's second law, without any artificial corrections imposed by thermostats, referred to as the Newtonian region.

MD simulations are performed to investigate the plastic deformation of the crystalline α - Al_2O_3 sample under nanoindentation using the open-source code LAMMPS [14]. All atomistic simulations are carried out using the Vashishta potential, which is used to compute α - Al_2O_3 material properties relevant for deformation mechanisms [13,15]. All calculations were performed with a radial cutoff distance of 6.0 \AA . In a previous study [13], we tested and compared the transferability of a large bench of rigid ion (RI), 2/3-body and variable charge potentials. Special attention was given to the characterization of material properties that are significant for nanomechanical applications including lattice and elastic properties, surface and stacking fault energies and dislocation properties. The RI formalism relied on Buckingham

potentials [16]. The 2/3-body potential was developed by Vashishta et al. [15] and consists of two- and three-body terms. The two-body term included steric-size effects, charge-induced dipole, fixed charged Coulomb and van der Waals interactions. The 3-body term relied on the angular interaction between Al-O-Al and O-Al-O triplets of atoms. The many-body SMTB-Q interatomic potential was a variable charge model originally created by Tétot et al. [17,18]. It was based on the charge equilibration QEQ method that allows for local ionic charge variations using the electronegativity equalization principle of Rappé et al. [19], which was the closest to the quantum theory and allowed for the *on-the-fly* evaluation of the ionic charge [20]. However, it has a higher cpu cost than the RI and 2/3-body formalisms and fails to use it to perform large-scale MD simulations. Based on the Ref. [13], we verified that the 2/3-body Vashishta potential was the best alternative to the more costly variable charge potentials with only slight discrepancies when compared to DFT and the experimental literature data. Moreover, in this study, the ReaxFF potential [21,22] was tested to verify the transferability of the results and was in the same family as the SMTB-Q, *i.e.*, the variable charge potentials, at the expense of wild CPU costs, which are not consistent with large-scale MD simulations, see Appendix A.

After preparation of the sample, the potential energy of the system is minimized using a force norm stopping criterion $f_n = 10^{-6} \text{ eV/\AA}$ to find the lowest energy structure. A thermalization procedure to 300 K is carried out under the Nosé–Hoover NPT (isobaric–isothermal) ensemble for a duration of 100 ps, ensuring that the complete system attains equilibrium, with a homogeneous temperature and pressure profile [23]. This process was continued by implementing an open boundary in the z-direction, allowing the system to stabilize and achieve a homogeneous temperature profile by applying a relaxation process for 10ps (see Appendix B). We ensured that the sample surface remained stable throughout the nanoindentation simulation, as any oscillations could potentially impact the Hertz description of the elastic process. Here, (0001), ($\bar{1}210$), (10 $\bar{0}0$) and (10 $\bar{1}2$) crystallographic orientations were used to model the nanoindentation tests. For the load along the one axis, periodic boundary conditions in the other two directions are applied, while that direction is set as the fixed boundary condition. Correspondingly, the load along the one of the orientations, are fixed boundary conditions, while the other two orientations are applied by periodic boundary conditions.

In our numerical modeling, a spherical indenter tip can be used to represent a Berkovich tip since there are minimal differences in the phase transformation regions of both tips during the initial loading stages and considering its roundness. Thus, we consider an imaginary repulsive spherical indenter tip as developed in our previous work [23]. The total force F exerted by the indenter on the sample is defined by $F = -K(\vec{r}(t) - R)^2$, with K being the force field constant or indenter tip stiffness set to 536 eV/\AA^3 according to experimental data [23]. $\vec{r}(t)$ and $R = 10 \text{ nm}$ refer to the position of the center of the tip as a function of time and radius, respectively. The velocity of the indenter is 20 m/s , while the time step is 0.001 ps (several different indenter tip sizes and strain rates were tested to verify the robustness of the MD results, see Appendix C). Here, $\vec{r}_t = x_0\vec{x} + y_0\vec{y} + (z_0 \pm vt)\vec{z}$. x_0 and y_0 present the center of the surface sample on the xy plane. z_0 (0.5 nm) is the initial gap between the surface and the indenter tip, avoiding the influence of the spherical tip on the top layer atoms. The loading and unloading processes are defined by considering the direction of the velocity as negative and positive, respectively. Each process is performed for 125 ps with a time step of $\Delta t = 1 \text{ fs}$. The maximum indentation depth is chosen to be 3.1 nm to avoid the influence of boundary layers in the dynamical atom region [24].

In this study, the mechanical response of the sample is investigated for various orientations and the Hertz model $F(\delta) = \frac{4}{3}E^*R^{\frac{1}{2}}\delta^{\frac{3}{2}}$, where E^* is an effective Young's modulus, $R = 10 \text{ nm}$ and δ is the indentation depth used to characterize the force response within the elastic regime of deformation. Elementary shear processes are investigated

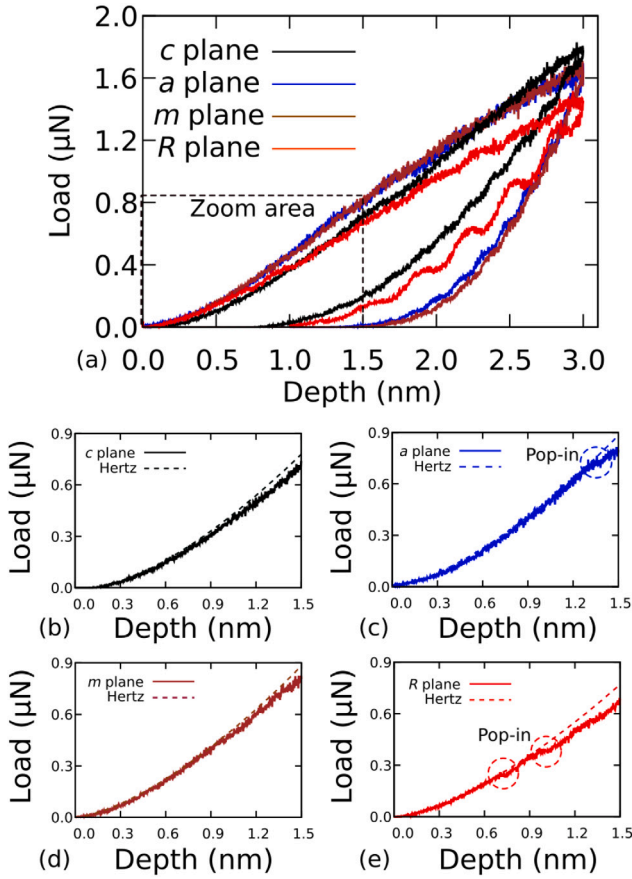


Fig. 2. Load vs. depth curves showing the loading and unloading process during four oriented nanoindentation tests. Hertz fitting is added to show the mechanical processes (dashed lines).

using Ovito's DXA and grain identification algorithms [25]. This numerical setup allows us to model the plasticity mechanisms during the early stages of nanoindentation loading properly, as discussed in Appendix E.

3. Results

3.1. Load–displacement curves

Fig. 2 shows load vs. depth curves for four orientations at RT, including m $[10\bar{1}0]$, a $[\bar{1}2\bar{1}0]$, R $[10\bar{1}2]$ and c $[0001]$. All samples are deformed up to $\delta = 3.0$ nm. The samples under nanoindentation show the maximum load for each orientation, and the corresponding order is $c > a \approx m > R$. Based on the load response, the curves can be described using the usual two deformation regimes. The elastic regime can be fitted well with the Hertz model, see the magnified area in Fig. 2(b)–(c). The load vs. depth curves for orientations a $[\bar{1}2\bar{1}0]$ and R $[10\bar{1}2]$ are characterized by observable pop-in events, while this event is minimal for the other two orientations. The initiation of the plastic deformation regime is marked by dislocation nucleation. Referring to the curves, pop-in events or load drops are observed. At this regime, a detailed analysis of Al_2O_3 dislocation-based mechanisms will be shown in the next section.

Table 1 presents the effective Young's modulus E^* and fitting intervals $[E^f]$, as well as critical load F_m with depth δ_m for the samples as a function of orientation. The results show that the largest yield load is obtained for the c plane, while the lowest yield load is obtained for the m plane. E^* values can be compared to the experimental bulk-alumina Young's modulus as presented [26–29].

Table 1

Effective Young's modulus E^* , Hertz fitting intervals $[E^f]$, critical load F_m , and depth δ_m for the $\alpha\text{-Al}_2\text{O}_3$ sample under indentation as a function of orientation. Experimental data are shown for comparison.

Orientations	E^* [GPa]	E^f [nm]–[nm]	F_m [nN]	depth δ_m [nm]
{0001} (c)	470 (461.00 [26])	0.20–1.65	0.78	1.6
$\{\bar{1}2\bar{1}0\}$ (a)	450 (431.24 [29])	0.20–1.35	0.47	1.0
$\{10\bar{1}0\}$ (m)	455 (431.20 [28])	0.10–1.41	0.33	0.8
$\{10\bar{1}2\}$ (R)	405 (386.10 [27])	0.12–0.40	0.38	1.0

3.2. Loading on the c plane {0001}

Fig. 3(a)–(b) shows the elastic deformation under indentation at the first stage. No dislocation is visible. Fig. 3(b) shows the phase transition. O atoms transfer from HCP atom structures into BCC and FCC atom structures. The phase transition is generated below the elastic region. It was not comparable with studies of Xu and collaborators [30]. They found that a phase transition was observed at the surface and center of alumina particles under nanocompression using atomistic simulations. Plastic deformation is characterized by nucleation of basal partial dislocations, as shown in Fig. 3(c). All partials are slipping by $\frac{1}{3}\langle 10\bar{1}0 \rangle$. Fig. 3(d)–(f) shows the growth of several rhombohedral twins $\{10\bar{1}2\}$ with increasing depth. A nanotwin is a planar defect in the crystal structure of a material that occurs along a twin boundary, separating two regions of the same crystal that are oriented in a mirror-like fashion. Notably, the presence of nanotwins in a material can lead to increased strength and ductility. In our material, the nanotwins grow in parallel and extend quickly. The enlarged atomic structure confirms that the angle between the nanotwin zone and indentation orientation is 58° . Twinning in the R plane is favored for this specific orientation, as shown by Sarobol et al. using microscopy and MD nanocompression [31]. In contrast to the slip systems depicted by Lin et al. [32], here, we do not observe the nucleation of pyramidal dislocations. The basal and rhombohedral twins dominate in the slip systems under nanoindentation. The Schmid's factor for the rhombohedral slip system is $M = 0.45$, which is the highest value for this orientation compared with other dislocation systems [33]. However, only R perfect dislocations (no twin) were characterized by Montagne et al. in *in situ* SEM micropillar experiments possibly due to the lower stress reached in the experiment induced by larger size samples (size-effect). When loading on the c plane {0001}, the observation of R twins is also in agreement with compression experiments performed in bulk $\alpha\text{-Al}_2\text{O}_3$ at 800°C by Lagerlof et al. [34].

3.3. Loading on the a plane $\{\bar{1}2\bar{1}0\}$

The elastic deformation process is observed at the first stage when loading on the a plane $\{\bar{1}2\bar{1}0\}$. However, the phase transition is around the elastic region, which is different from loading on the c plane, as shown Fig. 4(a). The first plastic deformation event occurs at a depth $\delta = 1.0$ nm and a loading force F of 0.47 μN . At this stage, a perfect pyramidal n dislocation nucleates from the contact zone, as shown Fig. 4(b). The dislocation propagates within a slip plane oriented at 64° from a plane, in line with the $(11\bar{2}3)$ pyramidal n plane proposed by the study of Lee and Lagerlof [35]. The Schmid's factor for the $(11\bar{2}3)$ pyramidal n slip system is $M = 0.38$, which is the favorable dislocation for this orientation. These observations are in good agreement with Kim et al. and Nishimura et al. MD nanoindentation for the same orientation [36,37]. However, pyramidal n dislocations quickly stop even increasing indentation depth. Therefore no pop-in event is observed. The basal partial dislocations occur along with gliding pyramidal n partial dislocations, as shown Fig. 4(c). The leading partial and trailing partial slip by $\frac{1}{3}\langle 10\bar{1}0 \rangle(0001)$. As the depth increases, the basal partial dislocations become the prominent slip system for this orientation. Therefore, the dislocations emerging are marked by pop-in events.

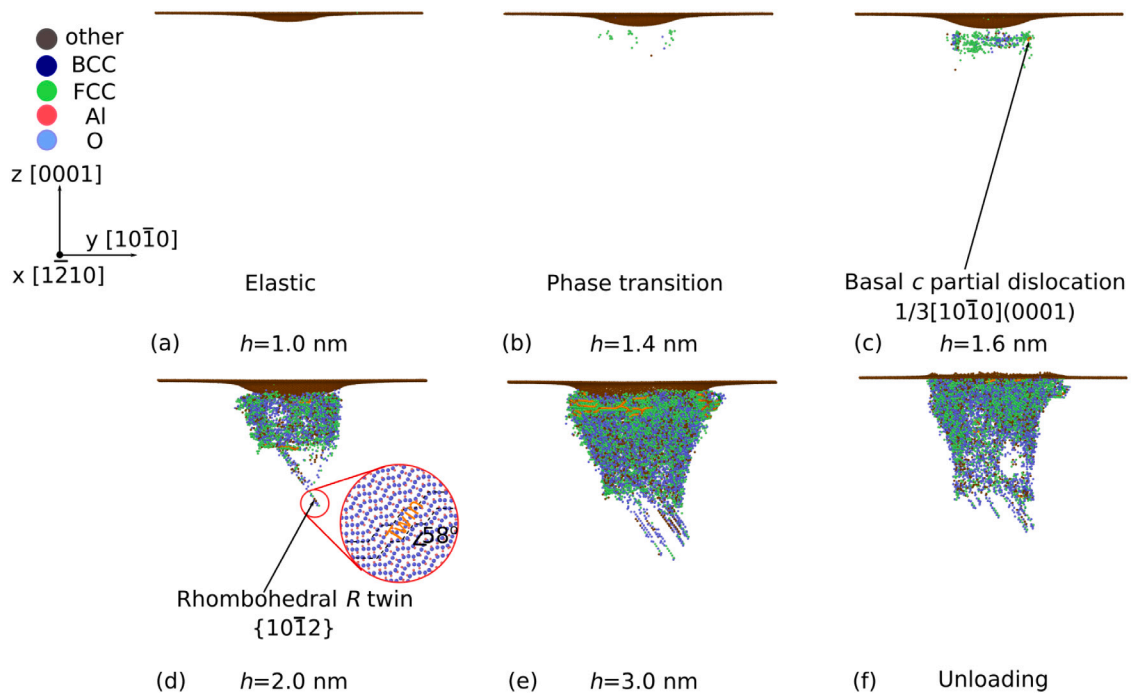


Fig. 3. Basal partial and rhombohedral twins nucleate in the α - Al_2O_3 sample under the indentation orientation of the c plane. Depth (a) $\delta = 1.0$ nm, (b) $\delta = 1.4$ nm, (c) $\delta = 1.6$ nm, (d) $\delta = 2.0$ nm, (e) $\delta = 3.0$ nm and (f) unloading position are shown. Sample cross-sections and atomistic configuration during nanoindentation are illustrated in the main figures without perfect crystal atoms. Only dislocation atoms are shown for the sake of clarity. They are colored blue, green or brown depending on the local crystal structure, *i.e.*, respectively. When they belong to the BCC and FCC defective regions, they are marked by blue and green. Surface atoms or twin boundary interfaces are colored brown. In the inset figures, both O and Al atom sublattices are shown in red and cyan, respectively. In addition, perfect dislocations are shown in green. Dislocations colored in orange refer to $\frac{1}{3}\langle 10\bar{1}0 \rangle$ dislocations.

At depth $\delta = 2.4$ nm, the rhombohedral R dislocation nucleated and temporarily cross-slips in a basal slip plane. The dislocations glide along the edge direction extending long screw segments, as shown Fig. 4(d) and (e). The rhombohedral R twin is generated from the corner of the surface with the plastic zone. The Schmid's factor for the rhombohedral R dislocation is $M = 0.50$, and the nucleation of R twins is also verified by compression experiments performed in bulk α - Al_2O_3 at 800 °C by Lagerlof et al. and Geipel et al. [34,38].

3.4. Loading on the m plane $\{10\bar{1}0\}$

For indentation along the m plane, the elastic deformation is comparable with indentation along the a plane. The primary dislocation nucleation occurs at $\delta = 1.0$ nm and at a loading force of $F = 0.34$ μN . These dislocations with Burgers vectors of type $\frac{1}{3}\langle 10\bar{1}0 \rangle$ nucleate and propagate in the c plane (see Fig. 5(b)). Again, the pyramidal n partial dislocation is visible and junctions with the existing basal dislocation. This is different from indentation along a plane, in which basal slip follows pyramidal n dislocation nucleation. Furthermore, the dislocation networks of basal and pyramidal n dislocations slip along orientation $[10\bar{1}0]$ with increasing depth. Then, rhombohedral twins form from the intersection of the surface and indenter contact area. The zone of atomic structure confirms that the slip system is a rhombohedral twin. The expansion of twins develops away from orientation $[10\bar{1}0]$ during plastic deformation. The $(1\bar{1}23)$ pyramidal n and R slip systems exhibit higher Schmid factors with $M = 0.43$ and 0.38 , respectively. Similarly, Kim et al. [39] also observed R slip for this orientation in MD simulations, similar to Montagne et al. in their alumina micropillar compression tests. R twins also remain consistent with observations performed in bulk when compressed along $[10\bar{1}0]$ [34].

3.5. Loading on the R plane $\{10\bar{1}2\}$

Fig. 6(a) shows that elastic deformation and phase transition are similar to loading on the c plane (0001). The beginning of plastic

deformation occurs at a depth of 1.0 nm. At this stage, dissociated $\frac{1}{3}\langle 1\bar{2}10 \rangle(0001)$ dislocations nucleate below the elastic region, as shown in Fig. 6(a). Fig. 6(b) shows that the dislocation is dissociated into leading $\frac{1}{3}\langle 1\bar{0}10 \rangle$ partial dislocations and trailing $\frac{1}{3}\langle 0\bar{1}10 \rangle$ partial dislocations separated by a stacking-fault (FCC atoms). The enlarged atomic structure shows that the slipping plane is located between two puckered Al layers without charge transfer, which is consistent with Bilde-Sørensen model for basal edge dislocations [40]. Heuer et al. [41] produced a markedly detailed atomic model of the dislocation cores with Al-Al terminated partial dislocations using the negative spherical-aberration imaging technique supporting the Bilde-Sørensen's model. Kronberg et al. proposed that slip occurs between two consecutive Al and O layers [42]. This slip model involves charge transport due to the ionic bonding between Al and O atoms. Shibata et al. [4] confirmed Kronberg's core hypothesis using high-resolution scanning transmission electron microscopy. As the load continues, several basal dislocations nucleate from the contact regions and cross-slip towards adjacent gliding planes (see Fig. 6(c)). Then, a rhombohedral twin occurs parallel to the surface, as shown in Fig. 6(d)–(f). again, the twin is verified with atomic structure. Basal c , Rhombohedral R and pyramidal n slip systems are characterized by $M = 0.25$, 0.46 , and 0.50 , respectively, which is consistent with our results. Again, all these dislocations were observed in Kim et al. MD nanoindentation simulations [36]. However, only cracks (no slip) were characterized by Montagne et al. in *in situ* SEM compression micropillar [33] and Roberts et al. tensile experiment [43], possibly related to the larger sample tested by the authors.

4. Discussion

This study investigates the deformation modes affected by four different crystallographic orientations in α - Al_2O_3 . Here, we present evidence of clear plastic deformation and phase transition. We can

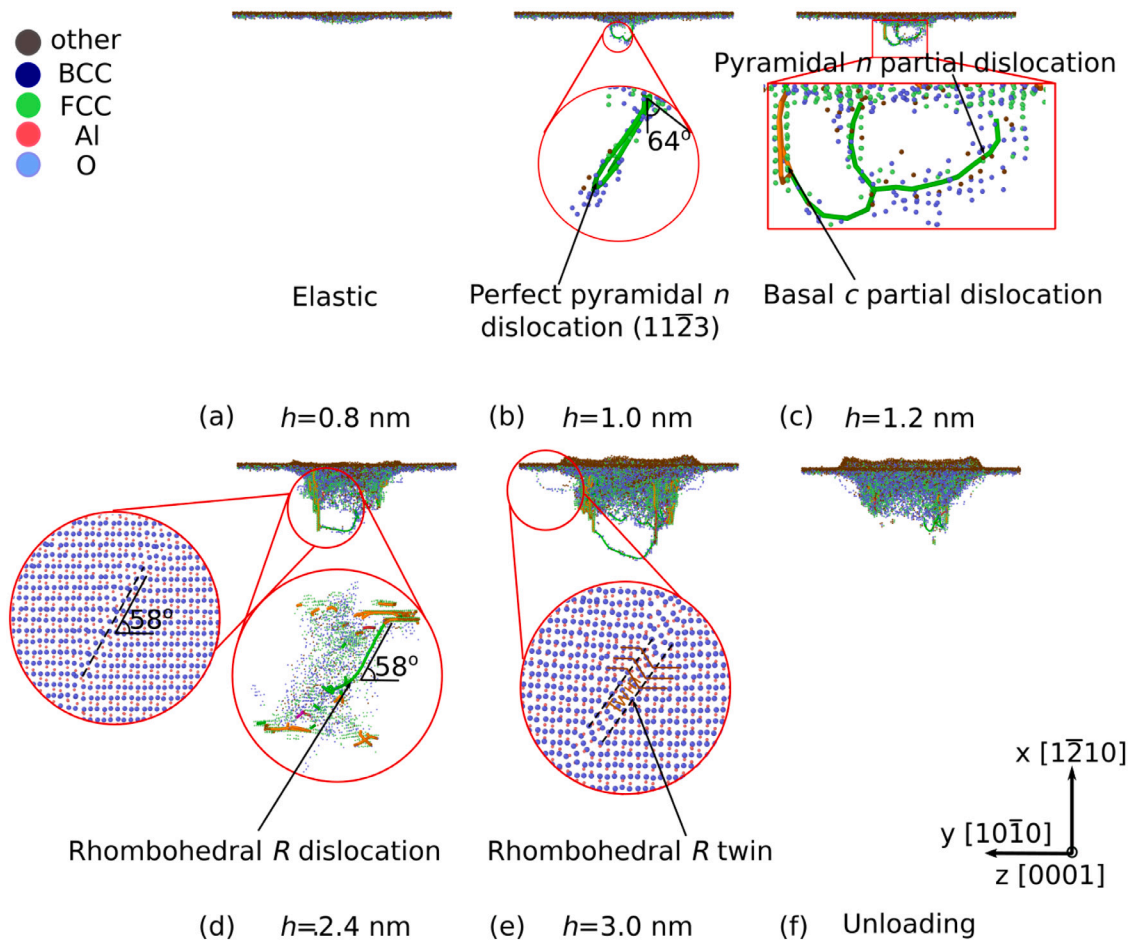


Fig. 4. Nanoindentation of the α -Al₂O₃ sample normal to the prism a plane. (a) showing elastic deformation. (b) Nucleation and propagation of a perfect $(11\bar{2}3)$ pyramidal n dislocation. (c) Nucleation and propagation of basal and pyramidal partial dislocations. (d)–(e) Nucleation and propagation of rhombohedral dislocations and twins. Additional information is provided in the caption of Fig. 3.

make several possible assumptions. (i) α -Al₂O₃ is a ceramic exhibiting a wide variety of deformation mechanisms including fracture, twinning, and dislocations. We detailed the nucleation of various slip systems under indentation. Four crystallographic orientations are investigated including m $[1\bar{1}00]$, a $[2\bar{1}\bar{1}0]$, R $[\bar{1}012]$ and c $[0001]$. We show that the deformation processes involve multiple dislocations including rhombohedral dislocations and twin $\{1\bar{1}02\}$, pyramidal n $\{11\bar{2}3\}$ and basal (0001) slip systems. This mechanical characterization is extremely remarkable compared with other ceramics and metal alloys. According to the MD simulation results, during the nanoindentation of c -plane sapphires, the first slip occurrence order was basal slip, followed by prismatic slip and pyramidal slip. Additionally, rhombohedral slip occurred in conjunction with basal and prismatic slips. Basal and prismatic slips were the dominant slip systems. Notably, the observed slip systems were consistent with those observed in the experiments. For instance, plasticity deformation process of MgO is only dominated by screw dislocation gliding in soft $\frac{1}{2}\langle 110\rangle\{110\}$ and hard $\frac{1}{2}\langle 110\rangle\{100\}$ slip systems when changing orientations and temperatures under pressure [44]. With regard to metal alloys, Feruz et al. used MD to study the strength of various FCC single crystal nanoparticles. They pointed out that the plastic regime starts when the Shockley partial dislocations nucleated at the vertices or corners of the nanoparticles [45]. Moreover, Montagne et al. studied the deformation processes of α -Al₂O₃ pillars using RT *in situ* SEM microcompression experiments [33]. Our MD results are consistent with Montagne's experiment at two orientations, including m $[1\bar{1}00]$ and c $[0001]$. The other two orientation results are different due to the size effect. (ii) In contrast to Schmid's law, active slip systems were not always those with the highest Schmid

factor. Schmid's law plays role when all slip systems contain mobile dislocations.

In this framework, Castaing et al. [46] investigated the mechanical properties of sapphire single crystals under compression within the temperature range of 25–1800 °C. They showed that the compression axis (CA) along the c axis or tilted 45° out leads to prismatic a (for $T > 200$ °C) and basal c (for $T > 600$ °C) slips, respectively. To characterize dislocation slip and twinning in sapphire, Lagerlof et al. [34] utilized TEM and observed prismatic a and m slips at temperatures as low as 200 °C for CA along c while more complicated processes, including basal and rhombohedral twinning, were shown to be dominant down to $T = 400$ °C for CA 45° off from $\langle 1\bar{2}10\rangle$. In a relevant study by Geipel et al., rhombohedral twins were observed in α -Al₂O₃ single crystals for CA parallel to the $\langle 2\bar{1}10\rangle$ direction at 600 °C. Sarbol et al. investigated the plasticity of defective and defect-free alumina micro- and nano-pillars (NPs) under compression using *in situ* TEM experiments and MD simulations [31]. For single crystalline NPs under compression along $[0001]$ at RT, dislocation nucleation initiated from the contact area (between the indent and NPs) within the rhombohedral slip system whereas bicrystals demonstrated reorganization of atoms near the contact between the indent and the grain boundary prior to fracture. After deformation, the authors showed that the NP fractured and split into two separated parts. No dislocation nucleation was observed in the bicrystal NP simulations. Performing *in situ* TEM nanoindentation experiments, Miao et al. pointed to dislocations associated with the $\frac{1}{2}\langle 11\bar{2}0\rangle(0001)$ basal slip as important contributions to the plastic deformation of alumina at elevated temperatures [47]. Montagne et al. studied the deformation processes of α -Al₂O₃ pillars

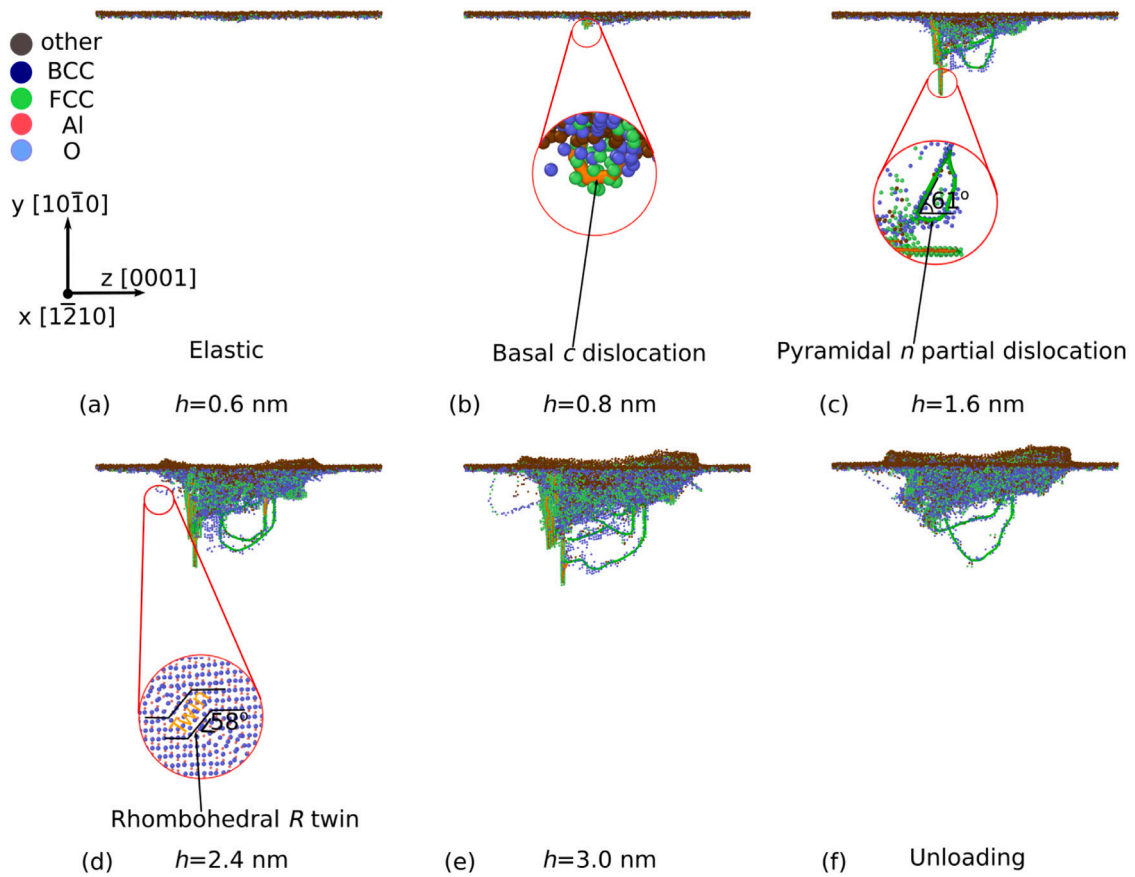


Fig. 5. Basal, pyramidal n partial and rhombohedral twins nucleate in the α - Al_2O_3 sample under the indentation orientation of the m plane. Depth (a) $\delta = 0.6$ nm, (b) $\delta = 0.8$ nm, (c) $\delta = 1.6$ nm, (d) $\delta = 2.4$ nm, (e) $\delta = 3.0$ nm and (f) unloading position are shown. Additional information is provided in the caption of Fig. 3.

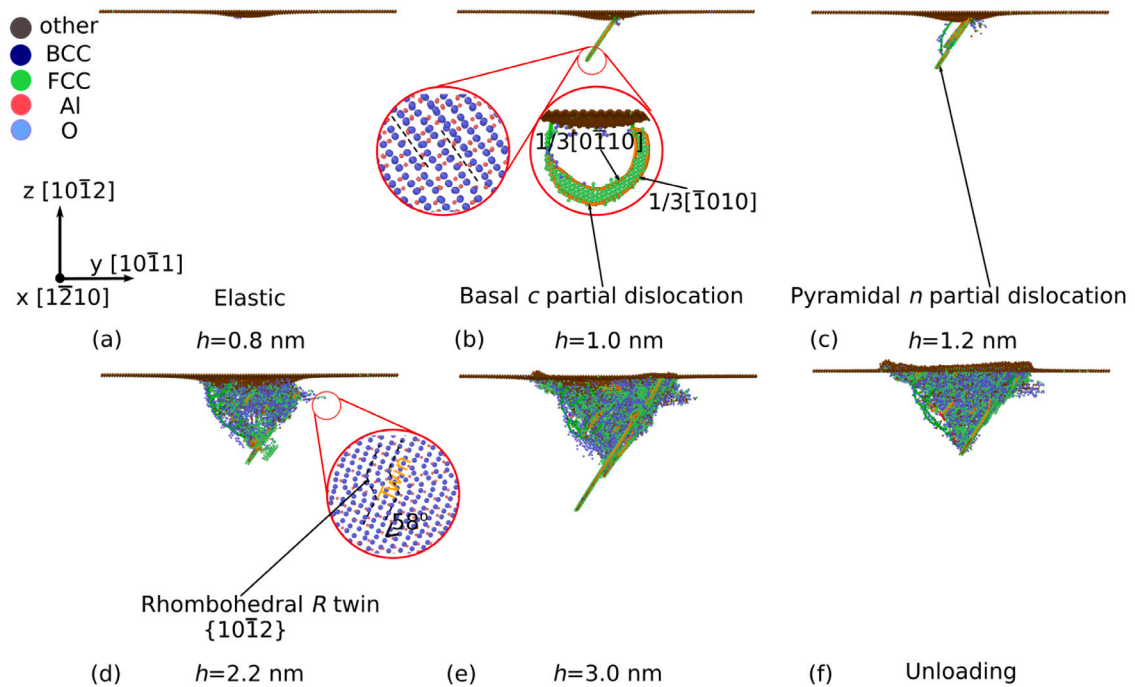


Fig. 6. Nanoindentation of α -alumina sample normal to the rhombohedral R plane. (a) Elastic deformation. (b) Nucleation and propagation of the basal partial dislocations. (c) Pyramidal n partial dislocation. (d)–(f) Nucleation of rhombohedral twins. Only O atoms are shown for the sake of clarity. Additional information is provided in the caption of Fig. 3.

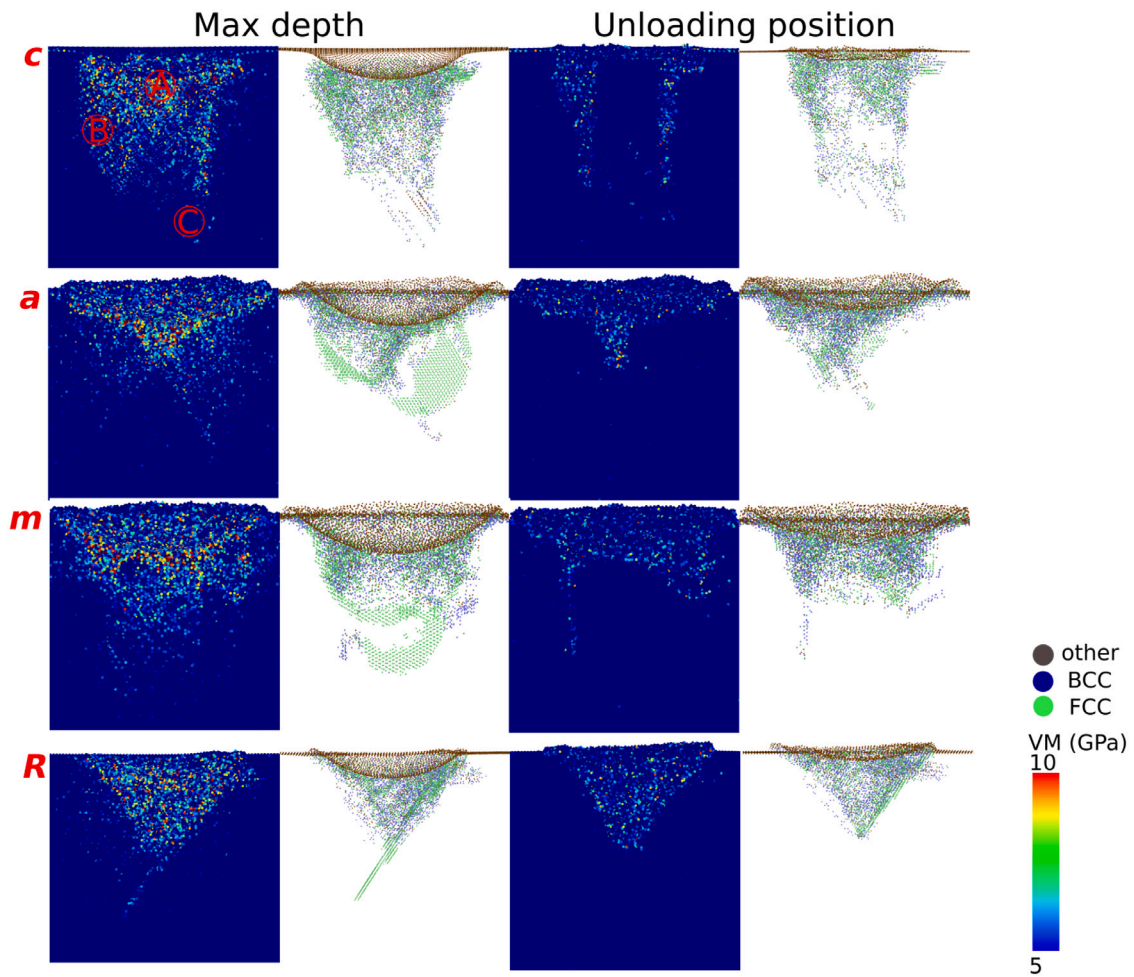


Fig. 7. The defect evolution and the corresponding von Mises stress distribution of the α -Al₂O₃ sample at depth $\delta = 3.0$ nm and unloading position.

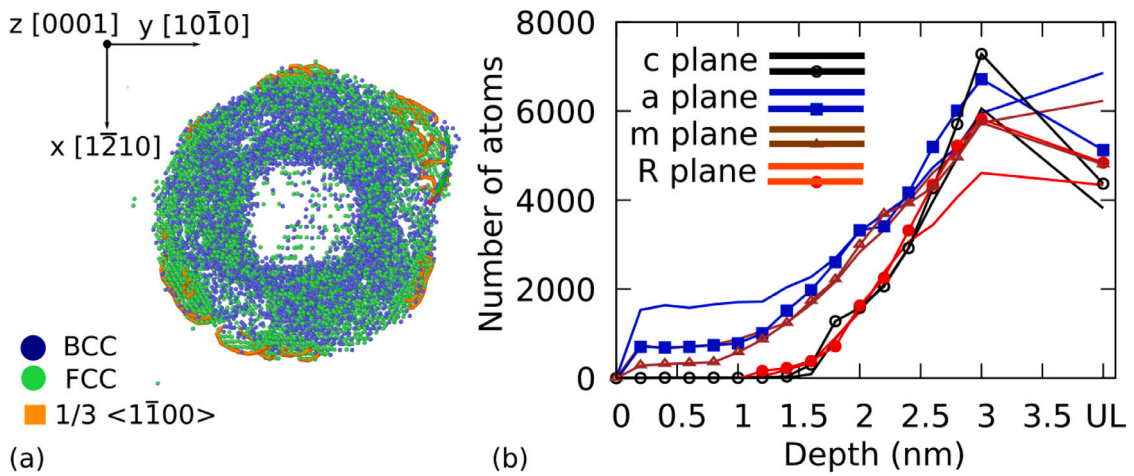


Fig. 8. The distribution of BCC and FCC atoms from Z view at depth $\delta = 3.0$ nm under indentation norm to c plane and the number of BCC and FCC as function of nanoindentation depth and unloading position (UL). Colored solid lines refer to the number of FCC. Colored line points refer to the number of BCC.

using *in situ* scanning electron microscopy (SEM) microcompression experiments at room temperature [33]. Four crystallographic orientations were investigated, including m $[1\bar{1}00]$, a $[2\bar{1}\bar{1}0]$, R $[\bar{1}012]$ as well as c $[0001]$. The authors show that the deformation processes of α -Al₂O₃ micropillars depend on the orientation with multiple slip-systems involved including rhombohedral $\frac{1}{3}\langle\bar{1}101\rangle\{1\bar{1}02\}$ and $\frac{1}{3}\langle 0\bar{1}11\rangle\{0\bar{1}12\}$ as well as pyramidal $\frac{1}{3}\langle 0\bar{1}11\rangle\{1\bar{1}01\}$ slip systems.

Table 2 summarizes relevant studies of plastic deformation associated with α -alumina including various orientations, temperatures, mechanical tests, and characterization techniques. As a future study, we plan to directly compare our MD results relevant to the dynamics of dislocations and their collective nature with electron microscope-based observations to be carried out in a local facility. To this end, the slip trace formation will be compared (quantitatively and qualitatively)

Table 2

Plastic deformation process observed in α -Al₂O₃ as a function of orientation, temperature and technique. For indentation tests, the orientation refers to the indented sample surface, while it corresponds to the compression/tensile axis in other cases.

Orientation	Temperature (°C)	Test/Analysis	Slip system	Reference
[0001] (<i>c</i>)	25 to 1800	Compression/SEM	Prismatic <i>a</i> and basal <i>c</i> slips	[46]
	25 to 1500	Tensile/SEM	Pyramidal <i>s</i> slip	[48]
	900	Indentation/MD	Rhombohedral <i>R</i> and prismatic <i>m</i> slips	[39]
	400	Compression/SEM	Basal <i>c</i> slip and <i>R</i> twinning	[34]
	300	Indentation/MD	Prismatic, basal and pyramidal slips	[37]
	RT	Compression/SEM	Rhombohedral <i>R</i> slip	[33]
	RT	Compression/MD	Rhombohedral <i>R</i> slip	[31]
	10	Indentation/MD	Pyramidal <i>n</i> , basal <i>c</i> slips, rhombohedral <i>R</i> and <i>c</i> twinning	[49]
[11̄20] (<i>a</i>)	900 to 1300	Compression/TEM	Basal <i>c</i> slip	[50]
	600 to 1550	Compression/TEM	Rhombohedral <i>R</i> twinning	[51]
	900	Indentation/MD	Pyramidal <i>n</i> slip	[39]
	800	Compression/TEM	Basal <i>c</i> and rhombohedral <i>R</i> twinning	[34,52]
	300	Indentation/MD	Pyramidal slip	[37]
	RT	Compression/SEM	Pyramidal <i>s</i> slip	[33]
	RT	Compression/TEM	Basal <i>c</i> slip	[47]
	Low-T (−196)	Compression/TEM	Rhombohedral <i>R</i> twinning	[38]
[10̄10] (<i>m</i>)	RT to 1500	Tensile	Fracture at directions [0001]	[43]
	600 to 1550	Compression/TEM	Basal <i>c</i> slip and twinning	[51]
	900 to 1300	Compression/TEM	Basal <i>c</i> slip	[50]
	900	Indentation/MD	Rhombohedral <i>R</i> and pyramidal <i>n</i> slips	[39]
	800	Compression/SEM	Basal <i>c</i> and rhombohedral <i>R</i> twinning	[34]
	700	Compression/TEM	Rhombohedral <i>R</i> twinning	[52]
	300	Indentation/MD	Prismatic slip	[37]
	RT	Compression/SEM	Rhombohedral <i>R</i> slip	[33]
[10̄12] (<i>R</i>)	RT to 1500	Tensile	Fracture at directions [11̄20] and [1̄012]	[43]
	900	Indentation/MD	Basal <i>c</i> , prismatic <i>a</i> , rhombohedral <i>R</i> , pyramidal <i>s</i> , <i>n</i> slips	[39]
	RT	Compression/SEM	Fracture at direction [21̄10]	[33]

with SEM images of indented samples, and trends of hardness versus depth will be further investigated to provide insights into the plasticity mechanisms at play. The above discussions have been included in the revised version of the manuscript.

As discussed above, dislocation nucleation governs the plasticity mechanisms not dislocation gliding. Hence, one might expect that a low Schmid factor system with a low critical nucleation load will activate one system to the next. This phenomenon is also confirmed by our results. For indentation along the *R* orientation, the first plastic event is basal partial dislocation ($M = 0.25$) not pyramidal *n* ($M = 0.50$) and rhombohedral ($M = 0.46$). Fig. 7 shows the von Mises stress distribution, which is comparable to the dislocation evolution. Concerning the von Mises stresses, the atoms of zone A exhibit high von Mises stress with a value of more than 9.0 GPa due to the concentrated load. Moreover, the intersection zone B of basal dislocations also has a high von Mises stress with a range from 7.5 GPa to 8.5 GPa. The gliding rhombohedral twins (zone C) exhibit lower von Mises stress below 5.0 GPa. A similar tendency is observed for other orientations. After unloading, the von Mises stress of zone A is close to 0 GPa due to the load off. However, the high von Mises stress is visualized because of the stable dislocation network. (iii) Our results show that the O atoms undergo a phase transformation, changing from the HCP atomic structure to the FCC and BCC structures obtained by the Common Neighbor Analysis (CNA) method which used as an effective filtering method to classify atoms in crystalline systems [53,54]. The phase transition atoms are concentrated around the plastic zone and the contact area with the tip, see Fig. 8(a). Fig. 8(b) shows the number of BCC and FCC phases as a function of nanoindentation depth and unloading position (UL). We can note that BCC atoms are observed clearly along the *c* orientation. However, FCC atoms are much more even for these orientations except along the *R* orientation.

S. Roy et al. [55] performed MD simulations to investigate the sintering process and compared four interatomic potentials for α -Al₂O₃, including the Vashishta, Matsui [56], Bouhadja [57] and Streitz [58] potentials. A comparison of the amount of sintering showed that only the Vashishta potential did not predict a significant amount of sintering at $T = 0.8T_m$ for all particle sizes. The Vashishta potential consisted of

two-body and three-body terms, and the latter part described triplets of atoms. The former was truncated at 6 Å, containing Coulomb interactions. This truncation failed to affect periodic systems. Also, in the case of free surfaces, it led to significant divergence, such as the pseudosize effects observed in the sintering of larger particles at higher temperatures. Therefore, the abrupt cutoff of Coulomb interactions was explained for this spurious behavior. This was why there was no sintering for particle sizes above $R = 2$ nm, even at the high temperature of $T = 0.8T_m$. Comparing the different nanodeformation mechanisms of α -Al₂O₃ is invaluable, and the follow-up work including the field testing is required to validate the finding of these studies.

5. Concluding remarks

In this work, we studied the plasticity of the α -Al₂O₃ sample under nanoindentation along four different crystallographic orientations, including *m* [1100], *a* [21̄10], *R* [1012] and *c* [0001] at room temperature. The results show that orientation along the *c* plane exhibited the largest maximum load force. When plastic deformation occurs in the slip systems, basal *c*, rhombohedral *R* and pyramidal *n* slips, as well *R* twinning are preferred. The results also show that the O atoms undergo a phase transition, changing from the HCP structure to the FCC and BCC structures. Usually, the *c* orientation will make it easier to observe the BCC and FCC atoms. The results are compared with the mechanisms of different nanodeformations, and are discussed in the light of recent simulations as well as microscopic observations.

CRediT authorship contribution statement

Qinqin Xu: Writing – original draft, Visualization, Software, Investigation. **Agata Zaborowska:** Formal analysis. **Katarzyna Mulewska:** Formal analysis. **Wenyi Huo:** Writing – review & editing, Writing – original draft, Conceptualization, Supervision. **Kamran Karimi:** Writing – review & editing, Investigation. **F. Javier Domínguez-Gutiérrez:** Writing – review & editing, Writing – original draft, Software, Investigation. **Łukasz Kurpaska:** Writing – review & editing. **Mikko J. Alava:** Writing – review & editing. **Stefanos Papanikolaou:** Writing – review & editing, Supervision, Methodology, Conceptualization.

Declaration of competing interest

The authors declare that they have no known competing financial interests or personal relationships that could have appeared to influence the work reported in this paper.

Data availability

Data will be made available on request.

Acknowledgments

We acknowledge support from the European Union Horizon 2020 research and innovation program under grant agreement no. 857470 and from the European Regional Development Fund via the Foundation for Polish Science International Research Agenda PLUS program grant No. MAB PLUS/2018/8. We acknowledge the computational resources provided by the High Performance Cluster at the National Centre for Nuclear Research in Poland.

Appendix A. Interatomic potential benchmark

The Vashishta potential, ReaxFF potential and the many-body variable charge SMTB-Q potentials were tested using a cell size of 25.2 nm \times 23.8 nm \times 27.7 nm (length \times height \times width, 1 936 620 atoms, perfect crystal) of α -Al₂O₃. The system was first relaxed and then subjected to a 1000 steps NVE MD run on a single cpu with 120 processors (3.50 GHz speed). Cpu times t and scaling factor t/t_V between each potential and the Vashishta simulation time are provided in Table A.3.

The total process are minimization, heat and indentation processes, over 420 000 steps. The ReaxFF is a potential that is (almost) of the same family than the SMTB-Q *i.e.*, the variable charge potentials, at the expense of wild cpu costs which are not consistent with large-scale MD simulations. By the way, as mentioned in the manuscript, Xu et al. 2022 Modeling Simul. Mater. Sci. Eng. 30035008 [13] had confirmed that Vashishta potential was the best among compared potentials. Moreover, Coleman et al. Acta Mat. 2014 [59], the authors show that the ReaxFF potential does not predict the α phase as the more stable Al₂O₃ phase with consequences on surface energy calculations especially for $T > 0$ K. The SMTB-Q has shown to be particularly suited in alumina with *e.g.*, the α -phase being the more stable but not suitable for large-scale MD simulations.

Appendix B. Initial zero stress conditions

Prior to nanoindentation simulation, the samples undergo an energy minimization process employing a conjugate gradient algorithm with an energy tolerance set at 10^{-6} eV. Subsequently, a thermalization procedure is carried out under the Nosé–Hoover NPT (isobaric–isothermal) ensemble for a duration of 100 ps, ensuring the complete system attains equilibrium, with a homogeneous temperature and pressure profile. Following this, the computational cell is expanded by 5 nm to accommodate a vacuum region positioned above the sample along the z direction. The sample is then subjected to a relaxation process lasting 10 ps, effectively eliminating any excessive heat accumulated during the sample preparation phase. In Fig. B.9 we show homogeneous zero von Mises stress profile of the initial sample.

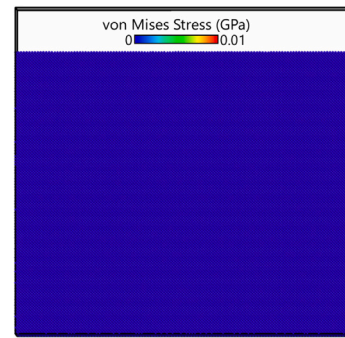


Fig. B.9. The initial zero von Mises stress conditions of the prepared α -Al₂O₃ sample prior nanoindentation test.

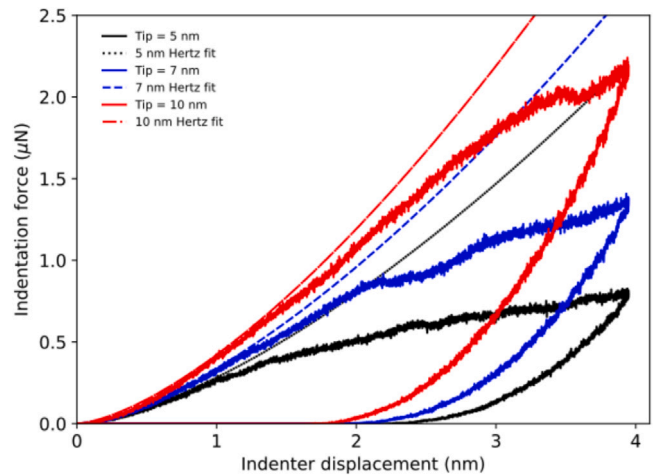


Fig. C.10. Load vs. depth curves showing the loading and unloading process for three indenter tips sizes under nanoindentation tests. Hertz fitting is added to show the mechanical processes (dashed lines).

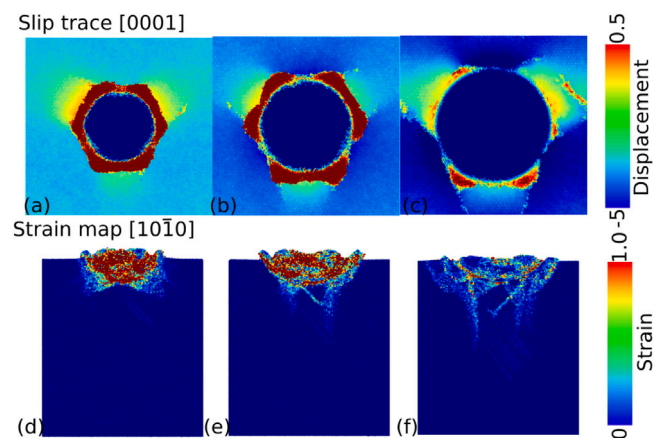


Fig. C.11. Slip trace along direction [0001] and Strain map along direction [10 $\bar{1}$ 0] for three indenter tips sizes under nanoindentation tests.

Appendix C. Indenter tip sizes and strain rates

Regarding the robustness of our results with respect to tip size effects and strain rates, we tested three different sizes of the indenter tip (diameter 10 nm, 14 nm and 20 nm) and various indenter velocities (10 m/s, 20 m/s, 50 m/s and 100 m/s). Overall, our key observations including the indentation-induced phase transformation and activation of different slip mechanisms are fairly robust with respect to the range

Table A.3

Cpu times t and scaling factor between each potential and the Vashishta time t/t_V for 1000 steps MD run (1 936 620 atoms) performed on a single cpu.

	Vashishta	ReaxFF	SMTB-Q
t [s]	733	9287	251 313
t/t_V	1	~12.7	~342.9

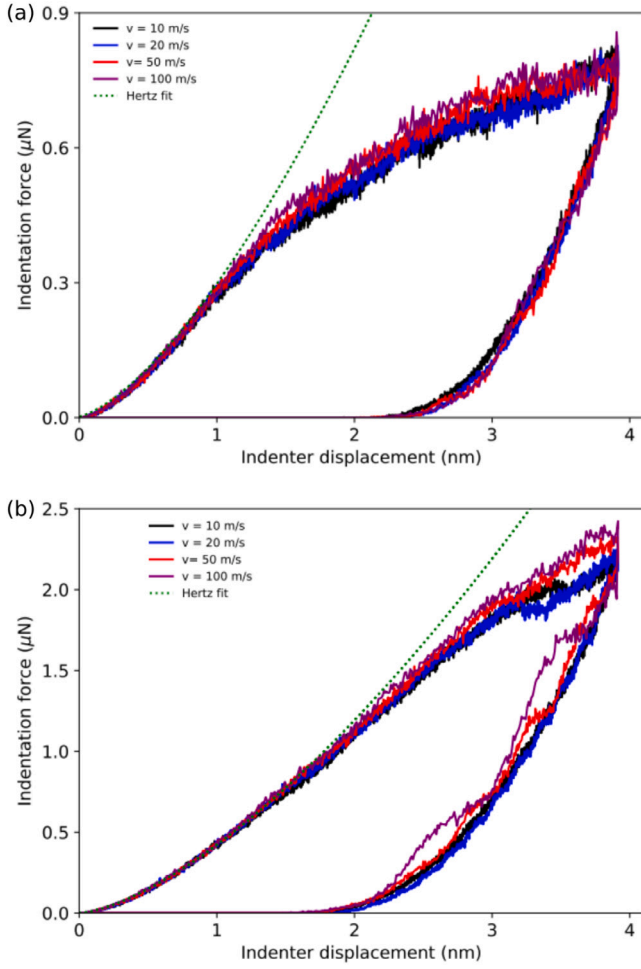


Fig. C.12. Load vs. depth curves showing the loading and unloading process for two indenter tips sizes with three strain rates under nanoindentation tests. Hertz fitting is added to show the mechanical processes (dashed lines).

of the model parameters. We opted to present our data associated with the 20 nm tip and the indenter rate of 20 m/s in the main manuscript because in that case plastic deformation tends to initiate within the bulk (as opposed to the surface nucleation with the smaller radius). This allowed us to collect relevant data comparable with experimental observations by making fairly accurate estimates of the yield point/depth above which the material begins to nucleate defects in response to the applied stress (see Figs. C.10–C.13).

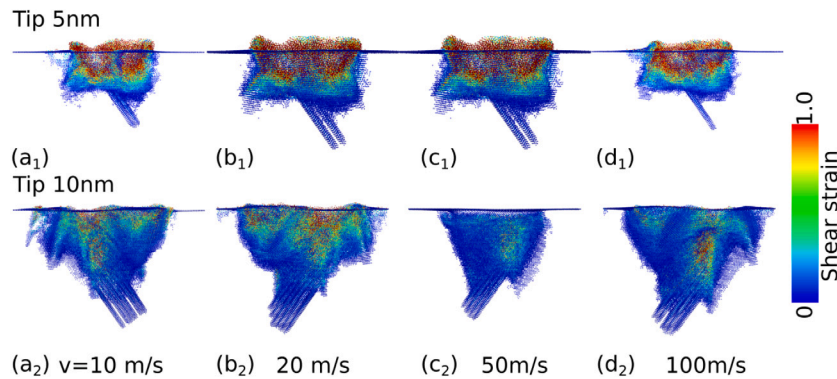


Fig. C.13. Stress strain viewed from $[1\bar{1}10]$ for two indenter tips sizes with three strain rates under nanoindentation tests.

Appendix D. Maximum shear stress

The influence of surface atom arrangement and thermally induced atomic vibrations on load–displacement curves has been well-established by Varilla et al. [60]. To minimize the impact of these fluctuations, a numerical setup was adopted in our work, maintaining a contact radius to indenter radius ratio of $a/2R \sim 0.05$. To mitigate the effects of these fluctuations, a numerical setup was chosen to maintain a ratio of $a/2R \sim 0.05$ between the contact radius and indenter radius. This approach ensures that the results exhibit minimal variation, typically less than 5% with a tip radius of 10 nm that fulfills this requirement and enables enhanced dislocation interactions.

It is crucial to recognize that plastic deformation does not initiate at the material's surface but rather at a depth beneath it known as the yield point or yield depth. It is within this region that defects and dislocations start to form in response to applied load or stress. Accurately capturing this behavior necessitates appropriate modeling of interatomic potentials. Specifically, the plastic deformation process occurs in the immediate plastic region beneath the spherical indenter tip along the vertical z -axis. These insights into the methodology employed contribute to a comprehensive understanding of the experimental observations as reported in our previous work [24]. Thus, we compute the nanoindentation applied stress as:

$$\sigma_1 = - \left(\frac{3F}{2\pi a(h)^2} \right) \left[\left(1 - \left| \frac{z}{a(h)} \right| \arctan \left| \frac{a(h)}{z} \right| \right) (1 + \nu) - \frac{1}{2(1 + z^2/a(h)^2)} \right], \quad (\text{D.1})$$

as an attempt to determine the strength and stability of the alumina surface under load. The stress applied in the direction parallel to the indenter surface is then expressed as:

$$\sigma_2 = - \left(\frac{3F}{2\pi a(h)^2} \right) \frac{1}{1 + z^2/a(h)^2}, \quad (\text{D.2})$$

where ν denotes the Poisson's ratio, the nanoindentation load is represented by F which highly depends on the utilized interatomic potential. The maximum shear stress (τ_{Max}) that the material can sustain before undergoing plastic deformation is defined as $(\sigma_1 - \sigma_2)/2$ [24]. This value is normalized by the applied pressure, which is equivalent to the force F divided by the contact area. The dependence of the maximum shear stress on the normalized depth is shown in Fig. D.14, where the normalized depth is the distance from the material's surface to the point at which the maximum shear stress occurs, divided by the radius of the indenter responsible for applying the shear forces. Based on our molecular dynamics (MD) simulations, we observed that plastic deformation begins at a normalized depth of $z/a = 0.5$ for both temperatures investigated. Furthermore, the elastic process is accurately described, as evidenced by the behavior of aluminum (Al) and oxygen (O) atoms within the contact area. These atoms consistently

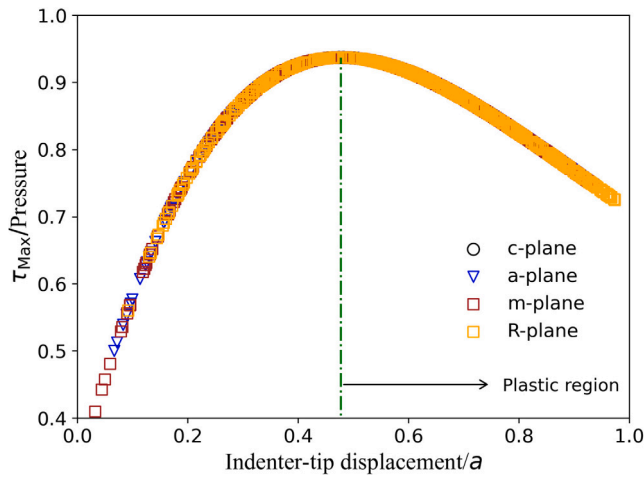


Fig. D.14. Hertzian calculation of normalized maximum shear stress by the applied pressure, τ_{Max}/P , as a function of normalized depth at the c-, a-, m-, and R-planes. The elastic part of the loading process is well modeled by our MD simulations, as observed in the range of 0.2 to 0.49 z/a .

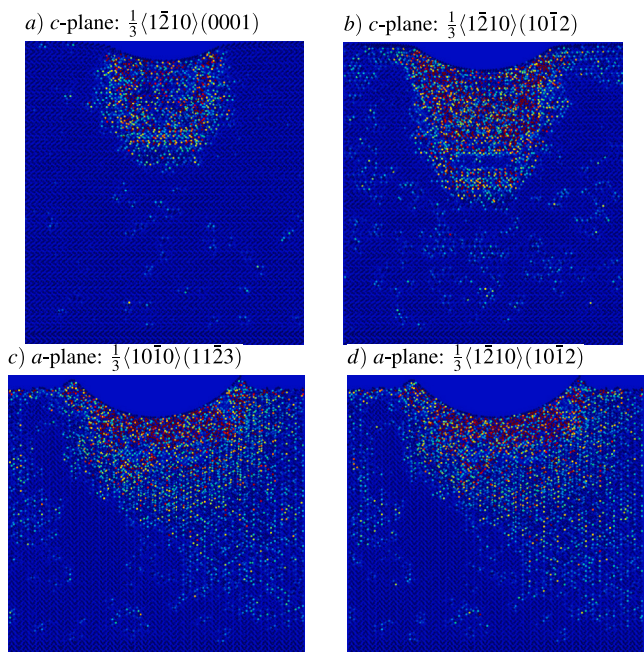


Fig. E.15. Shear stress τ_{RSS} resolved on the slip plane in the slip direction corresponding to the indentation on (a, b) c-plane (c, d) a-plane.

demonstrate the anticipated upward trend within the range of 0.0 to 0.4 z/a , regardless of the crystal orientation. This observation confirms an accurate representation of nucleation dislocation and pileup formation processes.

Appendix E. Resolved shear stress

To compute the (atom-wise) resolved shear stress (RSS), we consider active slip systems for individual atoms and project the local stress tensor $\sigma_{\alpha\beta}^i$ of atom i on relevant slip planes n along the slip directions t . Therefore,

$$\tau_{\text{RSS}}^i = t_{\beta} \sigma_{\beta\alpha}^i n_{\alpha}, \quad (\text{E.1})$$

where the Greek letters denote Cartesian indices. The results of our RSS analysis are presented in Fig. E.15.

References

- [1] E. Ramos-Moore, A. Rosenkranz, D.E. Diaz-Droguett, C. Espinoza, I. El Azahri, F. Muecklich, *Ceram. Int.* 48 (23, A) (2022) 34571–34575.
- [2] M. Magdy, Y.-B. Hu, J. Zhao, *Vacuum* 202 (2022) 111174.
- [3] B. Hockey, *J. Am. Ceram. Soc.* 54 (5) (1971) 223–8.
- [4] N. Shibata, M.F. Chisholm, A. Nakamura, S.J. Pennycook, T. Yamamoto, Y. Ikuhara, *Science* 316 (5821) (2007) 82–85.
- [5] K.-P. Lin, I. Stachiv, T.-H. Fang, *Mater. Res. Express* 4 (7) (2017).
- [6] C. Ferraro, S. Meille, J. Rethore, N. Ni, J. Chevalier, E. Saiz, *Acta Mater.* 144 (2018) 202–215.
- [7] W. Huo, F. Fang, X. Liu, S. Tan, Z. Xie, J. Jiang, *Appl. Phys. Lett.* 114 (10) (2019).
- [8] A. Olejarz, W.Y. Huo, M. Zielinski, R. Diduszko, E. Wyszowska, A. Kosinska, D. Kalita, I. Jozwik, M. Chmielewski, F. Fang, L. Kurpaska, *J. Alloys Compd.* 938 (2023).
- [9] C.T. Le, T.T. Nguyen, T.T. Nguyen, V.V. Le, *Vacuum* 167 (2019) 175–181.
- [10] K. Tsuruta, E. Tochigi, Y. Kezuka, K. Takata, N. Shibata, A. Nakamura, Y. Ikuhara, *Acta Mater.* 65 (2014) 76–84.
- [11] Z. Zhang, Z.H. Fu, R.F. Zhang, D. Legut, H.B. Guo, *RSC Adv.* 6 (16) (2016) 12885–12892.
- [12] T. Carisey, I. Levin, D. Brandon, *J. Eur. Ceram. Soc.* 15 (4) (1995) 283–289.
- [13] Q. Xu, N. Salles, J. Chevalier, J. Amodeo, *Modelling Simul. Mater. Sci. Eng.* 30 (3) (2022) 035008.
- [14] S. Plimpton, *J. Comput. Phys.* 117 (1) (1995) 1–19.
- [15] P. Vashishta, R.K. Kalia, A. Nakano, J.P. Rino, *J. Appl. Phys.* 101 (10) (2007) 103515.
- [16] J. Sun, T. Stirner, W. Hagston, A. Leyland, A. Matthews, *J. Cryst. Growth* 290 (1) (2006) 235–240.
- [17] R. Tétot, A. Hallil, J. Creuze, I. Braems, *Europhys. Lett.* 83 (4) (2008) 40001.
- [18] R. Tétot, N. Salles, S. Landron, E. Amzallag, *Surf. Sci.* 616 (2013) 19–28.
- [19] A.K. Rappe, W.A. Goddard III, *J. Phys. Chem.* 95 (8) (1991) 3358–3363.
- [20] N. Salles, O. Politano, E. Amzallag, R. Tétot, *Comput. Mater. Sci.* 111 (2016) 181–189.
- [21] S. Hong, A.C. van Duin, *J. Phys. Chem. C* 119 (31) (2015) 17876–17886.
- [22] S. Hong, A.C. Van Duin, *J. Phys. Chem. C* 120 (17) (2016) 9464–9474.
- [23] K. Mulewska, F. Rovaris, F. Dominguez-Gutierrez, W. Huo, D. Kalita, I. Jozwik, S. Papanikolaou, M. Alava, L. Kurpaska, J. Jagielski, *Nucl. Instrum. Methods Phys. Res. B* 539 (2023) 55–61.
- [24] F.J. Domínguez-Gutiérrez, P. Grigorev, A. Naghdi, J. Byggmästar, G.Y. Wei, T.D. Swinburne, S. Papanikolaou, M.J. Alava, *Phys. Rev. Mater.* 7 (2023) 043603.
- [25] A. Stukowski, K. Albe, *Modelling Simul. Mater. Sci. Eng.* 18 (8) (2010) 085001.
- [26] W. Mao, Y. Shen, C. Lu, *J. the European Ceramic Society* 31 (10) (2011) 1865–1871.
- [27] S. Graça, V. Trabadelo, A. Neels, J. Kuebler, V. Le Nader, G. Gamez, M. Döbeli, K. Wasmer, *Acta Mater.* 67 (2014) 67–80.
- [28] A.M. Goryaeva, P. Carrez, P. Cordier, *Phys. Chem. Miner.* 42 (10) (2015) 781–792.
- [29] L. Wang, Z. Hu, Y. Chen, Y. Yu, X. Xu, *Ceram. Int.* 46 (6) (2020) 7813–7822.
- [30] Q. Xu, *Dislocations and Nanomechanics in Alumina Using Atomistic Simulations* (Ph.D. thesis), Université de Lyon, 2021.
- [31] P. Sarobol, M. Chandross, J.D. Carroll, W.M. Mook, D.C. Bufford, B.L. Boyce, K. Hattar, P.G. Kotula, A.C. Hall, *J. Therm. Spray Technol.* 25 (1–2) (2016) 82–93.
- [32] J. Lin, F. Jiang, X. Xu, J. Lu, Z. Tian, Q. Wen, X. Lu, *Mech. Mater.* 154 (2021) 103716.
- [33] A. Montagne, S. Pathak, X. Maeder, J. Michler, *Ceram. Int.* 40 (1) (2014) 2083–2090.
- [34] K.P.D. Lagerlöf, A.H. Heuer, J. Castaing, J.P. Rivière, T.E. Mitchell, *J. Am. Ceram. Soc.* 77 (2) (1994) 385–397.
- [35] W. Lee, K. Lagerlöf, *J. electron microscopy technique* 2 (3) (1985) 247–258.
- [36] H.T. Kim, *Heat Transf.-Models Methods Appl.* (2018) 333–359.
- [37] K. Nishimura, R.K. Kalia, A. Nakano, P. Vashishta, *Appl. Phys. Lett.* 92 (16) (2008) 161904.
- [38] T. Geipel, K. Lagerlöf, P. Pirouz, A. Heuer, *Acta Metall. Mater.* 42 (4) (1994) 1367–1372.
- [39] W.K. Kim, D. Xi, B.H. Kim, *Comput. Mater. Sci.* 170 (2019) 109195.
- [40] J. Bilde-Sørensen, B. Lawlor, T. Geipel, P. Pirouz, A. Heuer, K. Lagerlo, et al., *Acta Mater.* 44 (5) (1996) 2145–2152.
- [41] A. Heuer, C. Jia, K. Lagerlöf, *Science* 330 (6008) (2010) 1227–1231.
- [42] M. Kronberg, *Acta Metall.* 5 (9) (1957) 507–524.
- [43] S. Roberts, H. Kim, P. Hirsch, *Strength of Metals and Alloys 1* (1993) 317.
- [44] J. Amodeo, P. Carrez, B. Devincere, P. Cordier, *Acta Mater.* 59 (6) (2011) 2291–2301.
- [45] Y. Feruz, D. Mordehai, *Acta Mater.* 103 (2016) 433–441.
- [46] J. Castaing, J. Cadoz, S. Kirby, *J. Phys. Colloq.* 42 (C3) (1981) C3–43.
- [47] B. Miao, S. Kondo, E. Tochigi, J. Wei, B. Feng, N. Shibata, Y. Ikuhara, *Scr. Mater.* 163 (2019) 157–162.
- [48] Ö. Ünal, K.P.D. Lagerlöf, *J. Am. Ceram. Soc.* 77 (10) (1994) 2609–2614.
- [49] C. Zhang, R.K. Kalia, A. Nakano, P. Vashishta, P.S. Branicio, *J. Appl. Phys.* 103 (8) (2008) 083508.

- [50] J. Castaing, A. Munoz, D.G. Garcia, A.D. Rodriguez, *Mater. Sci. Eng. A* 233 (1–2) (1997) 121–125.
- [51] J. Castaing, A. He, K. Lagerlöf, A. Heuer, *Phil. Mag.* 84 (11) (2004) 1113–1125.
- [52] Z.-M. He, X.-Q. Hu, Z.-X. Zhou, *Acad. J. First Med. Coll. PLA* 22 (10) (2002) 951–952.
- [53] J.D. Honeycutt, H.C. Andersen, *J. Phys. Chem.* 91 (19) (1987) 4950–4963.
- [54] D. Faken, H. Jónsson, *Comput. Mater. Sci.* 2 (2) (1994) 279–286.
- [55] S. Roy, A. Prakash, S. Sandfeld, *Modelling Simul. Mater. Sci. Eng.* 30 (6) (2022) 065009.
- [56] M. Matsui, *Mineral. Mag.* 58 (2) (1994) 571–572.
- [57] M. Bouhadja, N. Jakse, A. Pasturel, *J. Chem. Phys.* 138 (22) (2013).
- [58] F. Streitz, J. Mintmire, *Phys. Rev. B* 50 (16) (1994) 11996.
- [59] S.P. Coleman, D.E. Spearot, *Acta Mater.* 78 (2014) 354–368.
- [60] J. Varillas, J. Očenášek, J. Torner, J. Alcalá, *Acta Mater.* 217 (2021) 117122.